SUPPLEMENTARY INFORMATION

Resonant Energy Transfer Enhances Solar Thermal Desalination

Alessandro Alabastri[a,b,c,#], Pratiksha D. Dongare[a,b,c,d,#], Oara Neumann[a,b,d], Jordin Metz[b,c,e], Ifeoluwa Adebiyi[d,f], Peter Nordlander[a,b,d,g,*], and Naomi J. Halas[a,b,d,f,g,*]

[a]Department of Electrical and Computer Engineering; [b]Laboratory for Nanophotonics,; [c]Nanosystems Engineering Research Center for Nanotechnology-Enabled Water Treatment (NEWT); [d]Applied Physics Graduate Program; [e]Department of Chemistry, Rice University, Houston, TX 77005; [f]Department of Engineering, Houston Community College, Houston, TX 77082; and [g]Department of Physics and Astronomy, Rice University, Houston, TX 77005

[#]Equal contribution

[*]Correspondence to: nordland@rice.edu (P.N.), halas@rice.edu (N.J.H.)

Supplementary Note 1: Numerical Models

The basic modeling approach has been described and validated in previous works[1,2]. Briefly, Navier-Stokes equation is solved in the channels regions for laminar flows (the device operates in a low Reynold number regime). Diffusion equation is solved in the membrane region where both the effect of porosity and temperature are taken into account to describe the diffusion coefficient of water vapor within the membrane. Thermal transport equation is solved in all domains and include convective heat transfer within feed and distillate regions where fluids are present. All the details regarding the solved equations and the utilized temperature dependent parameter can be found in ref[1,2]. Here, we expand on the differences (mainly boundary conditions) among the geometries and thermal properties exposed in this work. In the following, Inlet flow rates (QF and QD) are considered at ambient temperature unless specified.

Model 1: utilized for Fig. 1 calculated data in the main text

Model 1 is utilized to replicate indoor experimental conditions. Feed and distillate enter the device at a temperature of 25 °C. Inflow boundary conditions have been utilized to take into account the heat flow through the inlet boundaries. The heat exchanger (orange region) is heavily insulated and, for simplicity, perfect insulation is assumed for this region. The experimental device is located on a cart made of steel which, given its high thermal conductivity can be considered as a heat sink with its temperature fixed at room temperature, 20 °C, used as boundary condition. The bottom surface of the polycarbonate case is fixed to the membrane with screws which hold the device at 5 mm from the top of the cart. The LEDs illuminate the device from a 10 cm distance but the glass of the LED lamp is placed at 5 cm from the top of the polycarbonate and it is heated by LEDs dissipation at a measured temperature of 40 °C which is used as boundary condition. Additional convective and radiative losses from the top polycarbonate surface have been included. Since LEDs are placed relatively close to the device a reduced convective contribute is expected and a convective coefficient $h = 0.1\ (W/m^2/K)$ has been chosen. An emissivity $\epsilon = 0.9$, similar to a black body, has been chosen to evaluate radiative losses. Convective and radiative losses have been neglected in the bottom region as the bottom surface of the polycarbonate layer reaches a temperature close to the heat sink fixed 20 °C boundary condition. All the lateral boundaries are considered thermally insulating since any loss can be neglected given the limited thickness of the domains compared to the lateral extension of the device.

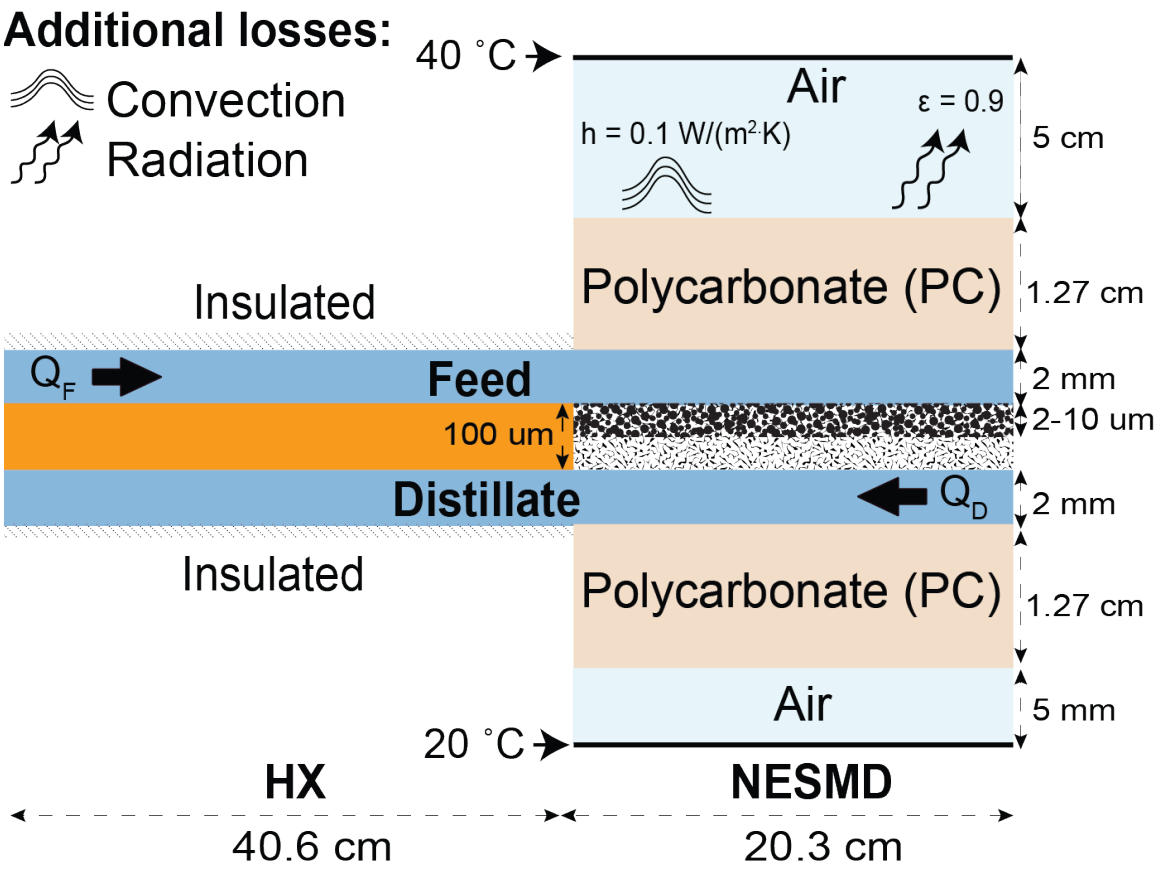

Supplementary Figure 1 – Schematic of the model utilized for Fig. 1 simulations

Model 2: utilized for Fig. 2a-d calculated data in the main text

The idea behind Fig. 2a-d was to estimate the performance of the experimental device outdoor and for different sizes. Therefore the model is the same as in the previous section with the exception of the varying size and boundary conditions. In particular, LEDs are replaced by sunlight intensity and the top polycarbonate surface now exchanges heat with the environment: a thick layer of air is considered ending with infinite elements to mimic outdoor conditions. Convective and radiative losses are referred to 20 °C outdoor temperature and $h = 5\ (W/m^2/K)$ is employed to simulate unforced natural convection.

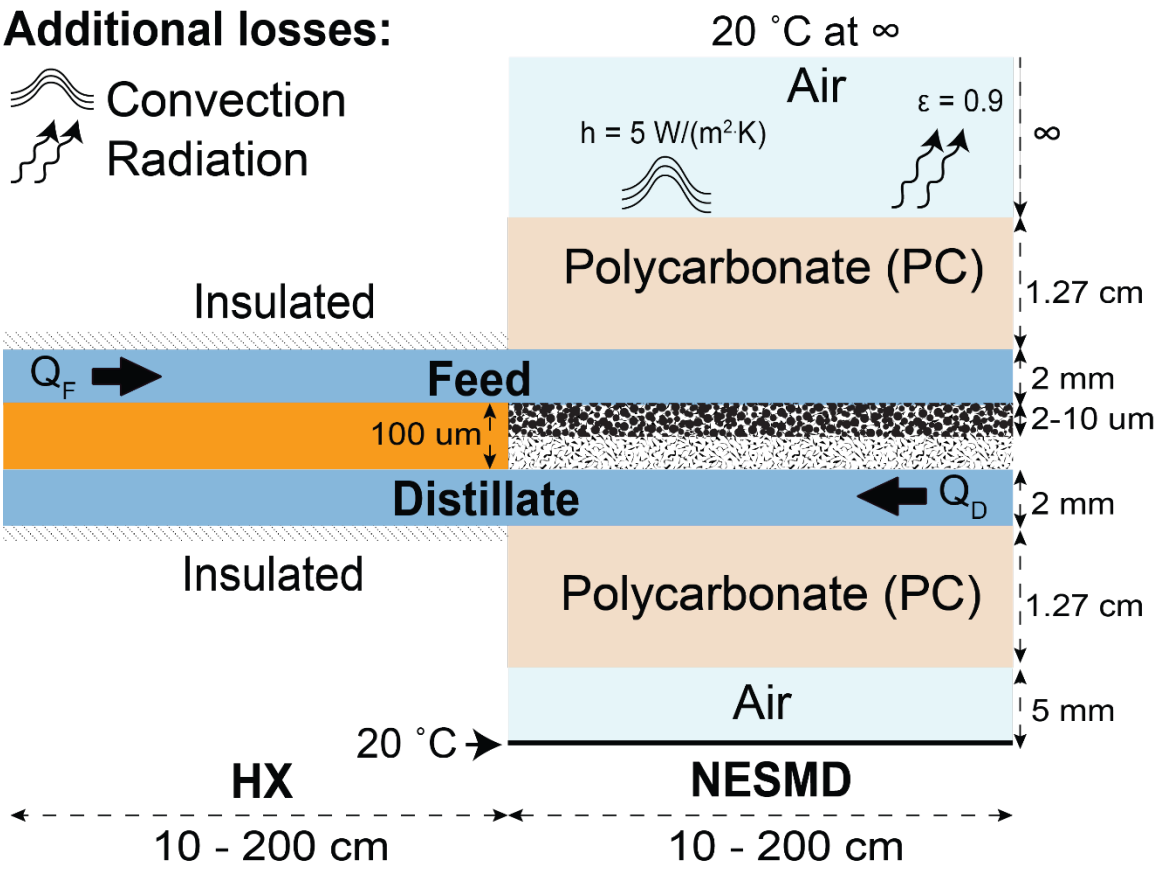

Supplementary Figure 2 – Schematic of the model utilized for Fig. 2a-d simulations

Model 3: utilized for Fig. 2e-f calculated data in the main text

The optimized model considered in Fig. 2e-f is based on the same principles of Model 1 and Model 2 with the following differences. The device is considered now placed on an aerogel base (more insulating than polycarbonate: $k_{aero} = 0.017\ (W/m/K)$ compared to $k_{poly} = 0.19\ (W/m/K)$. In order to minimize radiative losses, an infrared mirror is assumed to be placed on top of the polycarbonate top layer with an emissivity $\epsilon = 0.01$. Finally, to investigate the impact of potential losses in the heat exchanger region, a varying heat transfer coefficient $h_{coeff} = 0.1 - 5\ (W/m/K)$ has been chosen for both HX surfaces which are now assumed to dissipate heat with the environment at 20 °C.

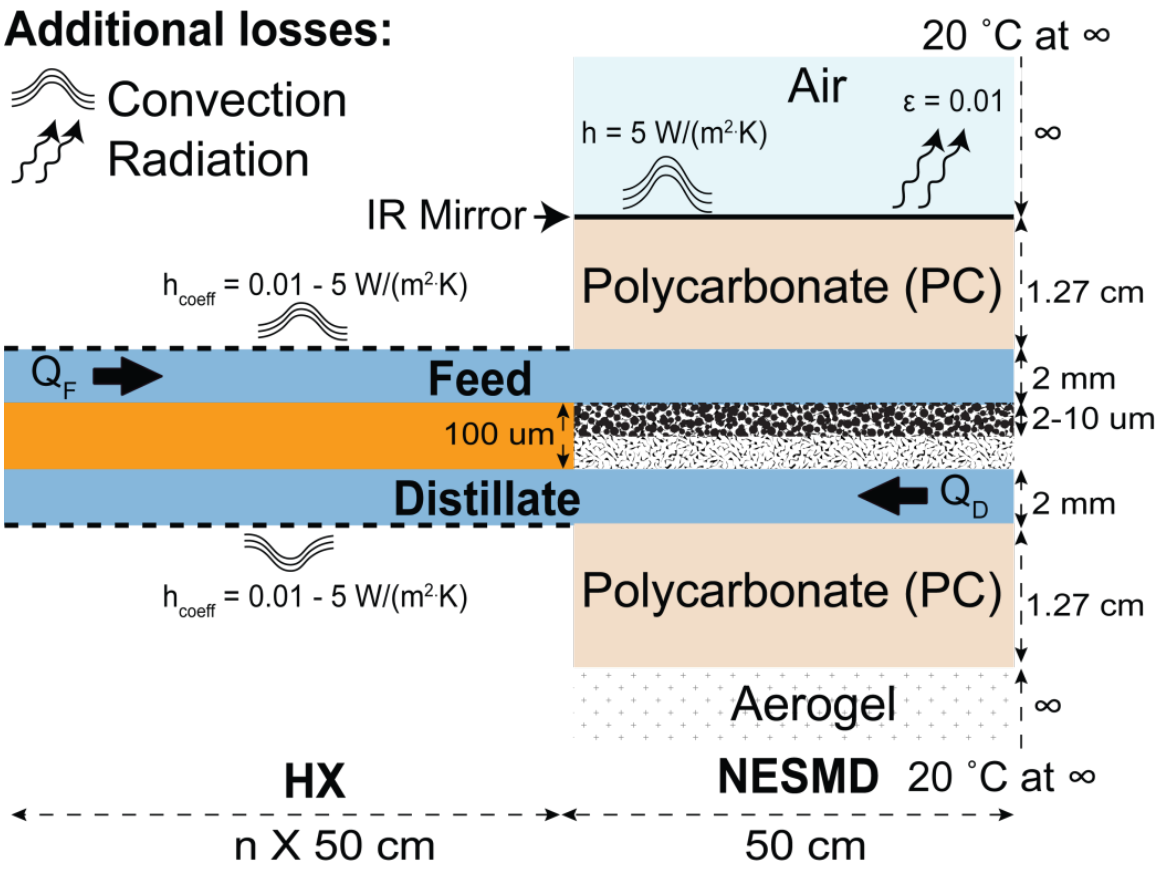

Supplementary Figure 3 – Schematic of the model utilized for Fig. 2e-f simulations

Equations utilized for Water flux calculations

The flux rate, expressed in kg/(m^2·h), is the main metric utilized in this work to compare different system configurations. At each point of the membrane, the transfer of water vapor from feed to distillate in the vertical y direction is defined by the spatially dependent molar flux, $f_y(x)$, expressed in $\left[\frac{mol}{m^2 \cdot s}\right]$ with x being the horizontal direction along the channels. The molar flux principally depends on the different saturation pressure on the opposite sides of the membrane and on the diffusion coefficient. It is generally calculated in its vectoral form in the (x, y) plane as:

$$\mathbf{f}(x, y) = -D\boldsymbol{\nabla} c(x, y)$$

where D is the diffusion coefficient of water vapor in the membrane that accounts for the porosity of the material and $c(x, y)$ is the concentration of water vapor, that is the variable for which the model solves (see ref[1], for additional details). Once the molar flux is calculated, the flux rate, F, as reported throughout this work, can be extracted as:

$$F = \frac{1}{L_{memb}} \int f_y(x) M_w dx$$

Where M_w is the molar mass of water, L_{memb} is the length of the active membrane and the integral runs over the total length of the membrane. The molar flux can be evaluated (with the proper sign) either at the feed or distillate side, since no vapor leaks are considered in the membrane. Even if the models are 2D, the 'third' dimension (lateral width of the membrane $d = 4\ in$) is taken into account for proper normalization.

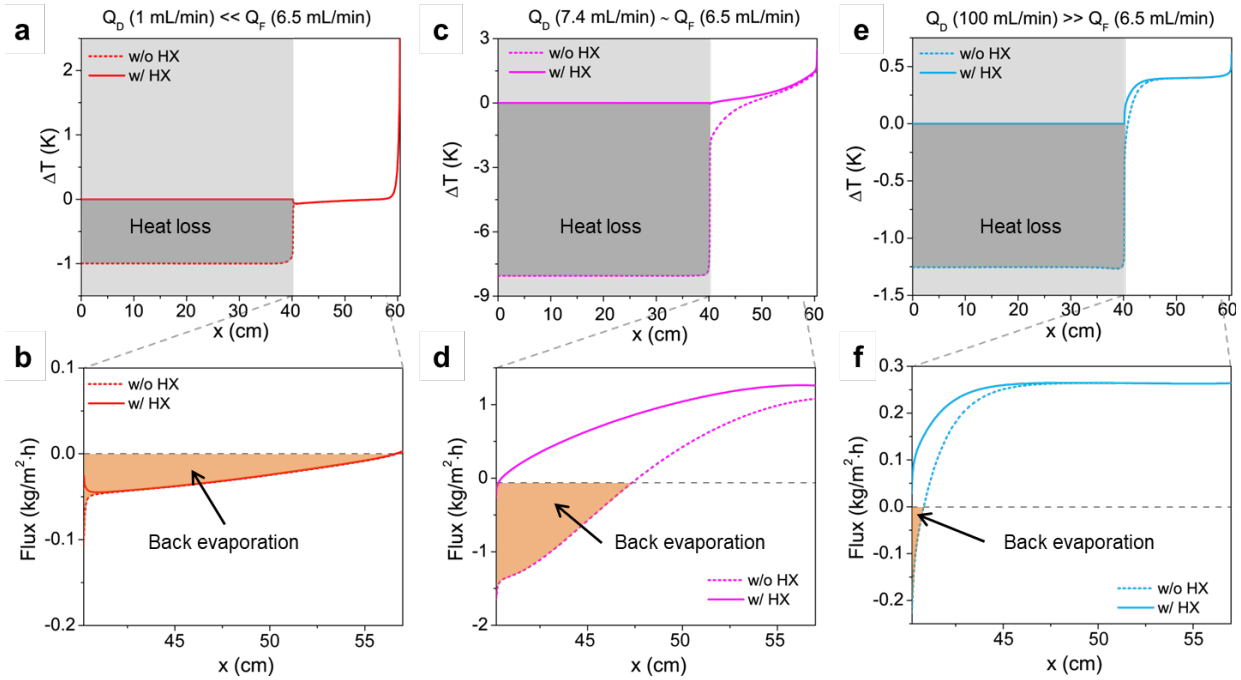

Supplementary Figure 4 - Temperature and flux analysis of NESMD with and without HX. a, Temperature difference along the length across the metal in 10.2 cm × 40.6 cm inline HX and 10.2 cm × 20.3 cm membrane in NESMD given by subtracting distillate temperature from the feed temperature (solid line). For the case without HX (dashed line), the metal in HX is replaced by an insulator with vanishing thermal conductivity ($\sim 10^{-9}$ W/(m · K)). The plots are shown in region of Q_D (1 mL/min) << Q_F (6.5 mL/min). **b**, The purified water flux through the membrane in NESMD with (solid lines) and without HX (dashed line) for Q_D (1 mL/min) << Q_F (6.5 mL/min). **c**, The temperature difference with (solid lines) and without HX (dashed lines) for Q_D (7.4 cm) ~ Q_F (6.5 mL/min). **d**, The flux through the membrane with (solid lines) and without (dashed lines) HX for Q_D (7.4 cm) ~ Q_F (6.5 mL/min). **e**, The temperature difference with (solid lines) and without HX (dashed lines) for Q_D (100 mL/min) >> Q_F (6.5 mL/min). **f**, The flux through the membrane with (solid lines) and without (dashed lines) HX for Q_D (100 mL/min) >> Q_F (6.5 mL/min).

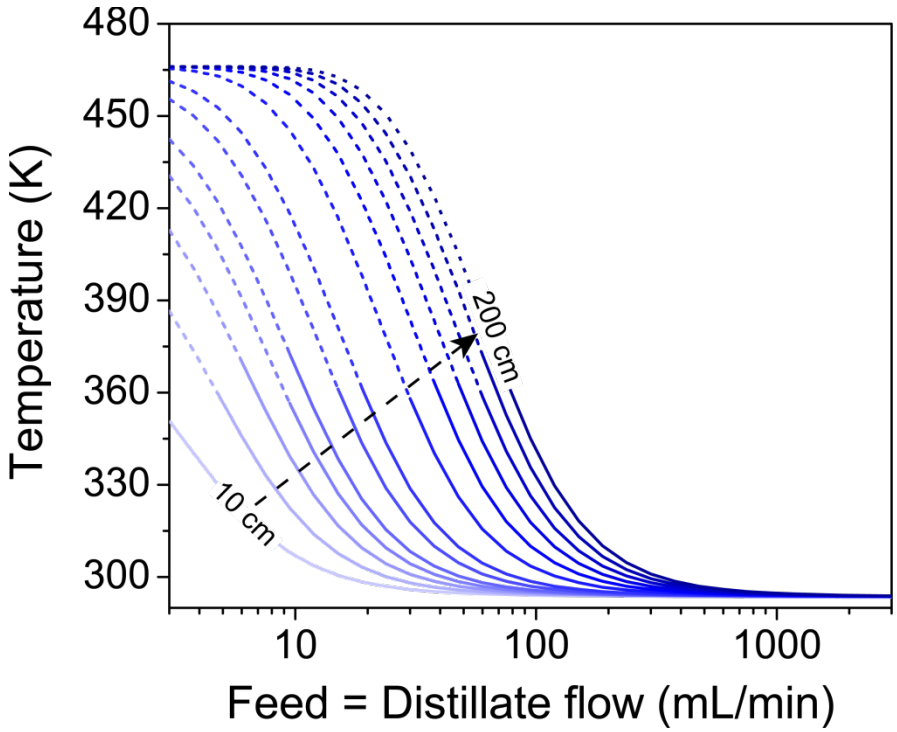

Supplementary Figure 5 – Maximum temperature in the system for different lengths. Maximum temperature in the TDO system with varying resonant feed and distillate flows for increasing NESMD module size from 10 cm to 200 cm with equal length of underlying HX layer.

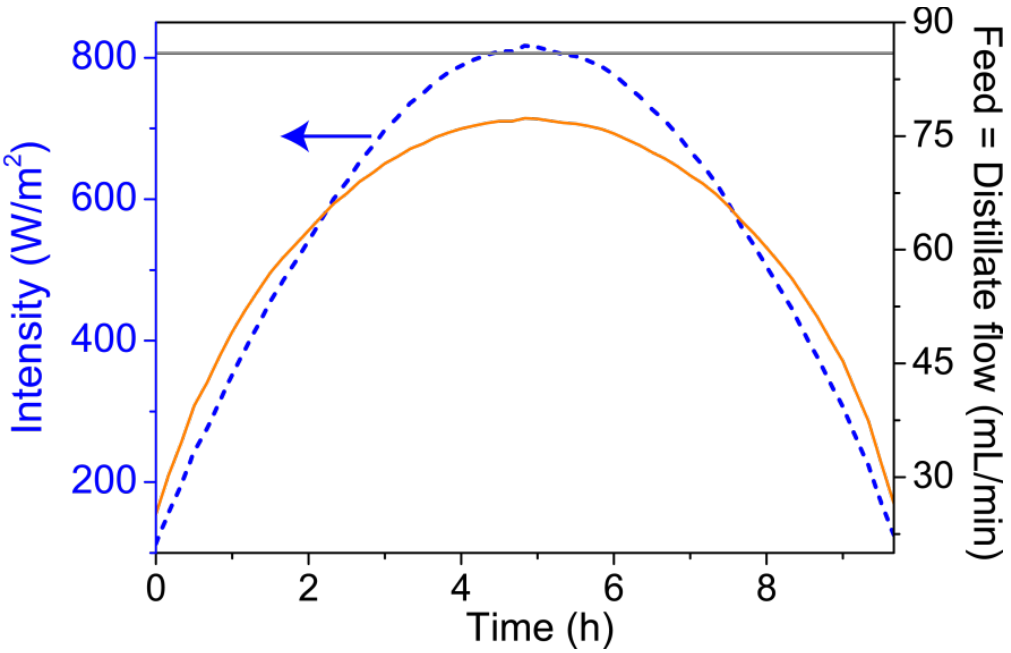

Supplementary Figure 6 –Static and dynamic resonance flows with intensity. The equal feed and distillate flows corresponding to the flux values shown in main text Fig. 2F for the static (grey line) and dynamic (orange line) flow control with varying incident light intensity (dashed blue curve) over a period of 9 hours during a typical sunny day.

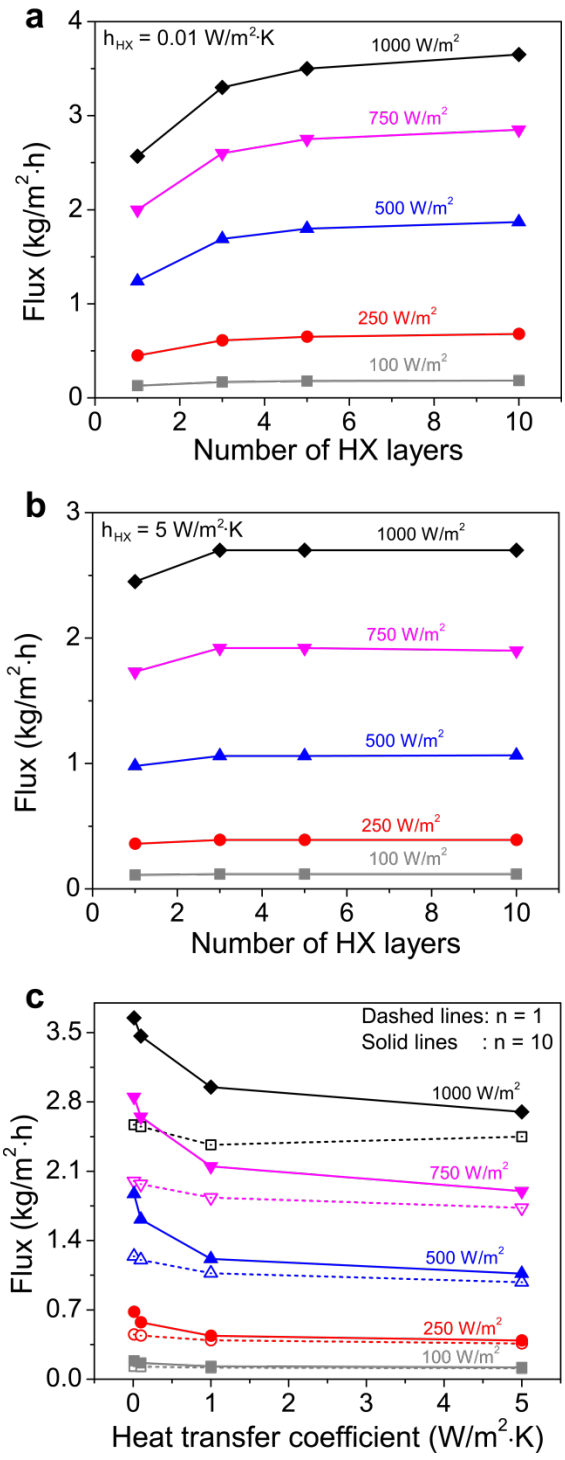

Supplementary Figure 7 - Performance analysis of TDO system with number of layers, intensity and losses. Flux production from NESMD system with 1 to 10 underlying HX layers considering heat transfer coefficient values of **a**, 0.01 W/m^2·K and **b**, 5 0.01 W/m^2·K under varying incident light intensity of 100 W/m^2 (grey), 250 W/m^2 (red), 500 W/m^2 (blue), 750 W/m^2 (magenta), and 1000 W/m^2 (black). **c**, Flux production from 1 (dashed lines) and 10 (solid lines) layered TDO system under varying solar intensity of 100 W/m^2 (grey), 250 W/m^2 (red), 500 W/m^2 (blue), 750 W/m^2 (magenta), and 1000 W/m^2 (black) with heat transfer coefficient h_{HX} varying from 0.01-5 W/m^2·K.

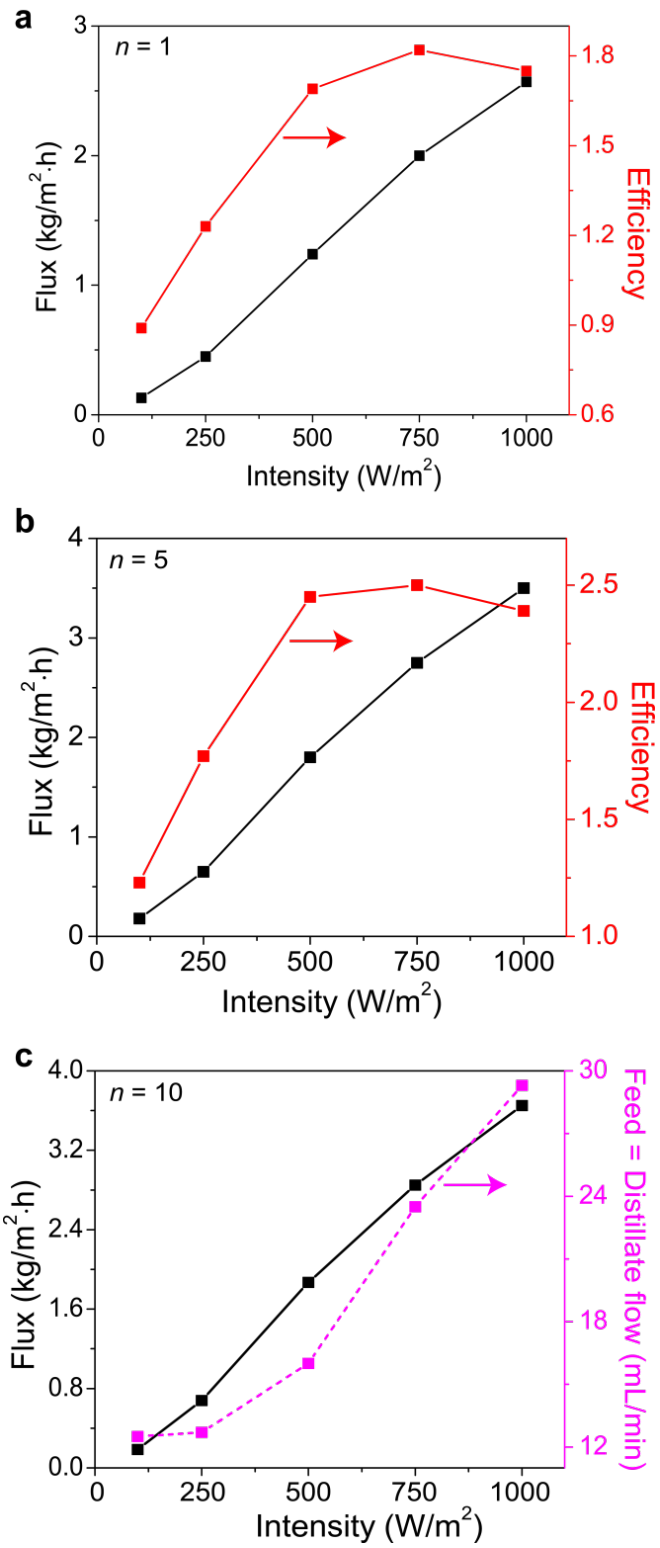

Supplementary Figure 8 - Performance analysis of 1,5,and 10 layered TDO system. Flux (black) and efficiency (red) variation with illumination intensity for **a**, 1 layered and **b**, 5 layered TDO system. **c**, The flux (black) and corresponding optimized feed and distillate flows (magenta) variation with illumination intensity for a 10 layered TDO system.

Supplementary Note 2: Effect of losses on optimal matched flows and maximum temperatures in a stacked system

Variation of heat transfer co-efficient (h_{HX}) in the finite element method simulation of the system allows us to study the effect of losses on the performance of the thermal desalination oscillator (TDO) system. Here we consider a stacked TDO system with 10 HX layers. We observe that as the losses in the system increase with increasing h_{HX} the optimized equal feed and distillate flow varies for a given light intensity as shown in Supplementary Figure 9a. For light intensities lower than 500 W/m^2 the optimized flow values increase with losses. This behavior can be explained from Fig. 2c and Supplementary Figure 5 where the maximum flux in the system is limited with the restriction of maximum temperature in the system not exceeding the boiling point of water. The maximum temperatures in the system for the varying intensities and losses in the system are shown in Supplementary Figure 9b.

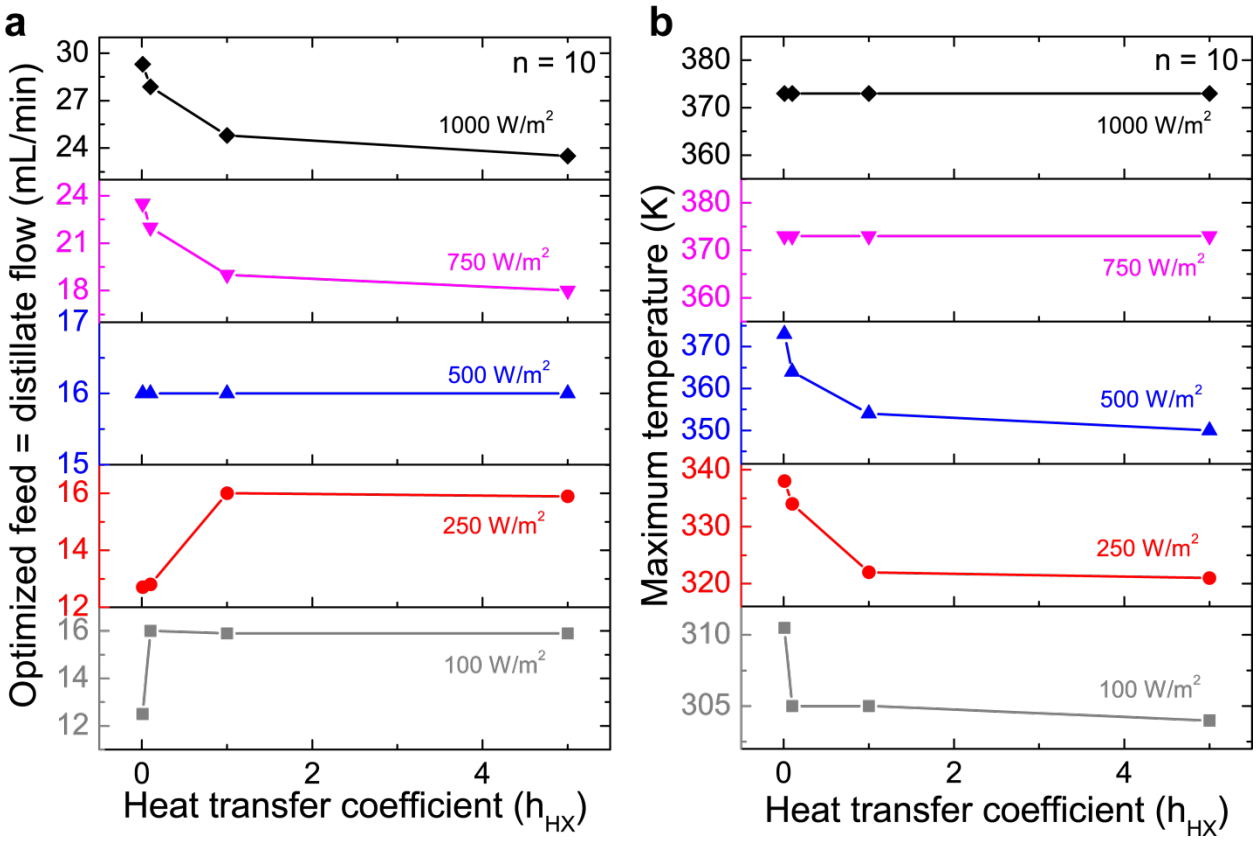

Supplementary Figure 9 – Effect of losses on the optimized feed and distillate flow in the system for NESMD with 10 HX layers. a, For a stacked 10 layer TDO system, the optimized feed and distillate flows in the system increase with increasing losses for lower intensities (<500 W/m^2) and reduce with increasing losses for higher intensities (>500 W/m^2). **b**, The corresponding temperatures in the system for varying intensities and losses.

Supplementary Note 3: Resonant heat transfer in counter-current flows: analytical solutions

Referring to Fig. 3a, the temperatures difference $T_F(x)$ and $T_D(x)$ along x in the channels (F and D) can be obtained by solving the following differential equations:

$$\begin{cases} \dfrac{dT_F(x)}{dx} = \dfrac{1}{\rho c w |u_F|}\left\{h_{eff}[T_D(x) - T_F(x)] + I_s\right\},\ T_F(-L/2) = T_{amb} \\ \dfrac{dT_D(x)}{dx} = -\dfrac{1}{\rho c w |u_D|}\left\{h_{eff}[T_F(x) - T_D(x)] + I_s\right\},\ T_D(L/2) = T_{amb} \end{cases}$$

With $T_F\left(-\frac{L}{2}\right) = T_D\left(\frac{L}{2}\right) = T_{amb}$. The terms on the right-hand side express the conditions of heat transfer between the channels (*i.e.* the coupling or interacting term) and heat accumulation from the source respectively. Despite the apparent simplicity of the equation, the explicit analytical solutions of $T_F(x)$ and $T_D(x)$ are relatively complex (see Supplementary Materials for details). However, these solutions can be utilized to calculate the heat transfers $I_{F\to D}$ and $I_{D\to F}$ pictured in Fig. 3a. For reasons that will become clear soon, we define:

$$\begin{cases} I_{F\to D} = \dfrac{2}{L}\displaystyle\int_0^{L/2} h_{eff}\Delta T(x)dx \\ I_{D\to F} = \dfrac{2}{L}\displaystyle\int_{-L/2}^{0} -h_{eff}\Delta T(x)dx \end{cases}$$

Here, $I_{F\to D}$ and $I_{D\to F}$ are the net heat transfers between feed and distillate for positive and negative x respectively (see Fig. 3b) and $\Delta T(x) = T_F(x) - T_D(x)$.

Their complete analytical solutions can be written as:

$$\begin{cases} T_F(x) = \dfrac{e^{-\frac{\alpha(L+2x)}{2}}\left\{I_s u_D[-2hL - \Sigma\phi] + e^{-\frac{\alpha(L-2x)}{2}}\left[h_{eff}u_f(I_s(L+2x) + \Delta\phi T_{amb}) + u_d e^{\alpha L}\left(h_{eff}I_s(L-2x) + \phi\left(h_{eff}T_{amb}\Delta + I_s\Sigma\right)\right)\right]\right\}}{\phi h_{eff}\Delta\left(u_d - u_f e^{-\alpha L}\right)} \\ T_D(x) = \dfrac{e^{-\frac{\alpha(L+2x)}{2}}\left\{I_s u_f[-2hL - \Sigma\phi] + e^{-\frac{\alpha(L-2x)}{2}}\left[h_{eff}I_s u_f(L+2x) + \phi u_f\left(h_{eff}T_{amb}\Delta + I_s\Sigma\right) + h_{eff}u_d e^{\alpha L}(I_s(L-2x) + \phi T_{amb}\Delta)\right]\right\}}{\phi h_{eff}\Delta\left(u_d - u_f e^{-\alpha L}\right)} \end{cases}$$

The temperature difference can be then written in the relatively compact form as:

$$\Delta T(x) = \frac{I_s}{h}\left\{\frac{\Sigma}{\Delta} - \frac{e^{\alpha(L-2x)}}{2}\left[2h_{eff}L + \phi\Sigma\right]}{\phi\left[e^{\alpha L}u_d - u_f\right]}\right\}$$

where, for clarity, we have defined: $\alpha = \frac{h_{eff}\Delta}{\phi u_D u_F},\ \Delta = u_D - u_F,\ \Sigma = u_D + u_F,\ \phi = cw\rho$

We can calculate now the net heat transfers as:

$$\begin{cases} I_{F\to D} = \dfrac{2}{L}\displaystyle\int_0^{L/2} h_{eff}[T_F(x) - T_D(x)]dx \\ I_{D\to F} = \dfrac{2}{L}\displaystyle\int_{-L/2}^{0} h_{eff}[T_D(x) - T_F(x)]dx \end{cases}$$

The complete analytical solutions (shown in Fig. 3b) are:

$$\begin{cases} I_{F\to D} = I_s \dfrac{h_{eq}\Sigma - \dfrac{2\left[-1 + e^{\frac{\alpha}{2}L}\right]u_D u_F\left[2h_{eff}L + \phi\Sigma\right]}{L\left[e^{\alpha L}u_D - u_F\right]}}{h_{eff}\Delta} \\ I_{D\to F} = I_s \dfrac{\left(\begin{array}{c} -h_{eff}Lu_D + 3h_{eff}Lu_F + 2\phi u_D u_F + 2\phi u_F^2 - \\ \dfrac{2\left[e^{\frac{\alpha}{2}L}u_D - u_F\right]u_F\left[2h_{eff}L + \phi\Sigma\right]}{e^{\alpha L}u_D - u_F} \end{array}\right)}{h_{eff}L\Delta} \end{cases}$$

Supplementary Note 4: Comparison with Lorentzian response

In order to proceed with the comparison with a typical Lorentzian response, it is convenient to recast the solutions using meaningful dimensionless parameters which describe the system:

$$\begin{cases} \gamma_D = \dfrac{h_{eff}L}{\phi}\dfrac{1}{u_D} \\ \gamma_F = \dfrac{h_{eff}L}{\phi}\dfrac{1}{u_F} \end{cases}$$

It is now possible to express the heat transfers as:

$$\begin{cases} I_{F\to D} = -I_s \dfrac{\gamma_D + \gamma_F - \dfrac{2\left(-1 + e^{\frac{\gamma_F - \gamma_D}{2}}\right)(\gamma_D + \gamma_F + 2\gamma_F\gamma_D)}{-\gamma_D + e^{\gamma_F - \gamma_D}\gamma_F}}{\gamma_D - \gamma_F} \\ \\ I_{D\to F} = I_s \dfrac{-\dfrac{1}{\gamma_D} + \dfrac{3}{\gamma_F} + \dfrac{2}{\gamma_F\gamma_D} + \dfrac{2}{\gamma_F^2} - \dfrac{\frac{2}{\gamma_F}\left(\frac{1}{\gamma_D}e^{\frac{\gamma_F - \gamma_D}{2}} - \frac{1}{\gamma_F}\right)\left(2 + \frac{1}{\gamma_D} + \frac{1}{\gamma_F}\right)}{\frac{1}{\gamma_D}e^{\gamma_F - \gamma_D} - \frac{1}{\gamma_F}}}{\frac{1}{\gamma_D} - \frac{1}{\gamma_F}} \end{cases}$$

By considering now a Lorentzian curve $L(\gamma_D, \gamma_F)$:

$$L(\gamma_D, \gamma_F) = \frac{1}{2} I_s \frac{\gamma_F^2}{(\gamma_D - \gamma_F)^2 + \gamma_F}$$

At 'resonance', the maximum temperature of the systems is reached at its center and can be written as:

$$T_{max} = T_F(0) = T_D(0) = \frac{1}{4} h_{eff} I_s \left(\frac{1}{u_d}\frac{L}{\phi}\right)^2 + \frac{1}{2} I_s \left(\frac{1}{u_d}\frac{L}{\phi}\right) + T_{amb} \text{ with } u_D = u_F$$

In fact, because of the symmetry of the system, the maximum increase (with respect to T_{amb}) is placed at the $x = 0$ and depends on two terms. One regards the coupled system and depends on the interaction between the channels, h_{eq}. The other one, intrinsic of the separate channels, depends on the heat source, I_s. While the former term scales with the inverse of the square of the velocity, the latter has an inverse dependence only. The relationship is consistent with what we found for heat transfers, since large circulating heat fluxes induce large stored thermal energy and thus high temperatures.

We can now compare it, for example, with the net heat transfer $I_{D\to F}$:

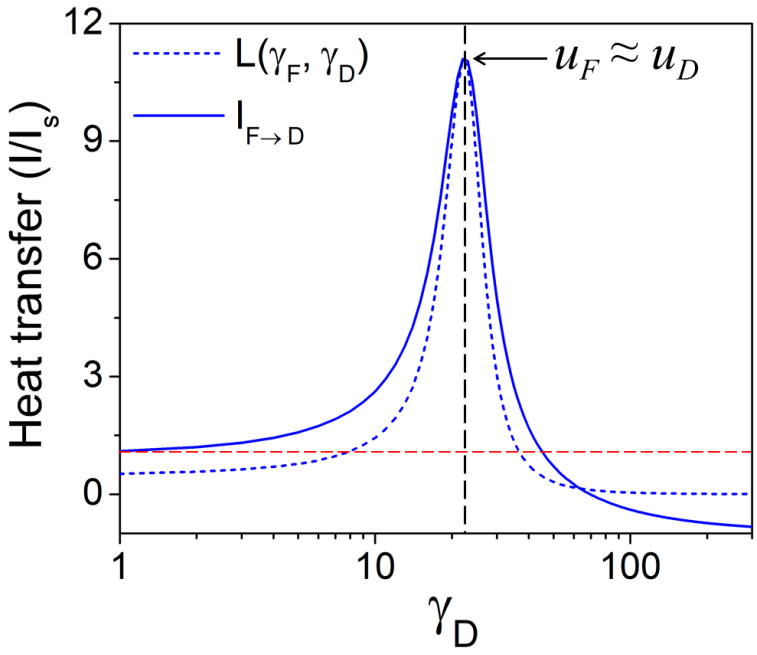

Supplementary Figure 10 - Heat transfer enhancements (normalized to I_s) of net heat transfers from F to D, $I_{F\rightarrow D}$ (solid, blue) depending on the velocity of D channel, u_D, parametrized as $\gamma_D = \frac{h_{eq}L}{\phi}\frac{1}{u_D}$ while $\gamma_F = \frac{h_{eq}L}{\phi}\frac{1}{u_F}$ is fixed. Utilized values are $h_{eq} = 200\frac{W}{m^2K}$, $L = 24\ in$, $c = 4.18\frac{kJ}{kg\,K}$, $\rho = 1\frac{g}{cm^3}$, $w = 2\ mm$, $u_F = 5.33\ 10^{-4}\frac{m}{s}$. The value of u_F corresponds to a flow value $Q_F = 6.5\ mL/min$ for a cross section of thickness w and width $d = 4\ in$. The overlap with a Lorentzian curve, typical of resonant systems, for $I_{F\rightarrow D}$, $L(\gamma_F, \gamma_D)$, is presented (dashed, blue).

Following up on the comparison with oscillating systems, we can also introduce an equivalent Q-factor (Q) of the system as the ratio between the total thermal energy (E_{tot}) and the lost heat (P_L) for the coupled channels. The total thermal energy increase in the system (E_{tot}) and the losses (P_L) can be written as:

$$\begin{cases} E_{tot} = cw\rho \int_{-L/2}^{L/2} T_F + T_D - 2T_{amb}dx \\ P_L = I_S L \end{cases}$$

At 'resonance', $u_D = u_F$, we obtain:

$$Q = \frac{E_{tot}}{P_L} = Q_{ext} + Q_{int} = \frac{1}{3}h_{eff}\frac{1}{cw\rho}\left(\frac{L}{u_d}\right)^2 + \frac{L}{u_d}$$

Again, one term of Q (which has time units) depends on the extrinsic coupling parameter h_{eff}, $Q_{ext} = \frac{1}{3} h_{eff} \frac{1}{cw\rho} \left(\frac{L}{u_d}\right)^2$, and scales as the inverse of the squared velocity. The other term is intrinsic of the channels, $Q_{int} = L/u_d$, and expresses the time it takes to the flow to go through the system, *i.e.* the natural heat accumulation time of the uncoupled system (dwell time). We can thus consider the coupling as a technique to enhance the natural accumulation of thermal energy and write:

$$\frac{Q_{ext}}{Q_{int}} = \frac{1}{3}\gamma \text{ with } \gamma = \gamma_D = \gamma_F$$

Moreover, being $\gamma \propto L/u$, this finding suggests the use of longer channels (larger L) to obtain stronger coupling for high-velocity flows (u). Intuitively, this can be understood from the fact that the heat vector field is less curved for large u values (when convection becomes dominant) and thus longer modules are needed for the spiral orbits to form.

Supplementary Note 5: Effect of losses on optimal matched flows: analytical solutions

The presence of the peak in Fig. 2c is explained by the presence of losses of the systems. Here we show how a simplified analytical model explains this behavior. The linear trend between optimal matched flows and size of the system can be also obtained and it is included in the analytical solutions below. Referring to the system of Fig. 3a, the temperatures in the channels are difference $T_F(x), T_D(x)$ along x in the channels (F and D) can be obtained by solving the following differential equation:

$$\begin{cases} \dfrac{dT_F(x)}{dx} = \dfrac{1}{\alpha|u|}\left\{h_{eff}[T_D(x) - T_F(x)] + I_s - g_{eff}T_F(x)\right\},\ T_F(-L/2) = 0 \\ \dfrac{dT_D(x)}{dx} = \dfrac{1}{\alpha|u|}\left\{h_{eff}[T_D(x) - T_F(x)] - I_s + g_{eff}T_D(x)\right\},\ T_D(L/2) = 0 \end{cases}$$

Where $|u_F| = |u_D| = |u|$ represents the matched flows (as it is in the cases shown in Fig. 2) and g_{eff} is an effective coefficient which identifies the external losses of each channels such as conduction and convection. While g_{eff} does not take into account losses non-linearly dependent

with temperature (*e.g.* radiation losses), we will show that these simplified loss mechanisms are sufficient to explain the peak shown in Fig. 2c.

Similarly to what was done in *Supplementary Note 2*, we can calculate the exchanged heat fluxes (now equal, due to symmetry) as:

$$I_{F\to D} = I_{D\to F} = \frac{8\, hI_s u\alpha \sinh\left(\frac{\sqrt{g(g+2h)}L}{4u\alpha}\right)^2}{gL\left[(g+2h)\cosh\left(\frac{\sqrt{g(g+2h)}L}{2u\alpha}\right)^2 + \sqrt{g(g+2h)}\sinh\left(\frac{\sqrt{g(g+2h)}L}{2u\alpha}\right)\right]}$$

The curves I/I_s with ($I_{F\to D} = I_{D\to F} = I$) are reported in the main text in Fig. 3c. The utilized parameters are: $I_s = 1000\, W/m^2$, $u = Q/A$ with $Q = 0.1\, L/min$, $A = wd$ and $w = 0.1\, L/min$, $d = 0.1\, m$, $h = h_{eff} = 200\, W/(m^2K)$, $g = g_{eff} = 10\, W/(m^2 \cdot K)$, $\alpha = \rho c w$ with $\rho = 1000\, kg/m^3$ and $c = 4180\, J/(kg \cdot K)$.

Supplementary Note 6: GOR calculations

According to the definition utilized in[3] the flux rate or SWP (Specific Water Productivity) can be defined as:

$$F = SWP = \frac{I_s}{H_{vap}}\eta_s GOR$$

Where I_s is the solar irradiation, H_{vap} is the latent heat of evaporation, $\eta_s = \eta_t \alpha$ is the solar utilization efficiency which includes the thermal efficiency η_t and the solar absorptivity α. Regarding the experimental setup reported in Fig. 1, the limit for a perfect single stage (no heat recovery, GOR=1) thermal desalination system is $F_{lim,NO-HX} = \frac{I_s}{H_{vap}} \sim 0.76\, kg/(m^2 h)$ with $H_{vap} \sim 2250\, kJ/kg$ and $I_s \sim 475\, W/m^2$. Given that, for the case without HX, we obtain $F_{exp,NO-HX} \sim 0.2\ kg/(m^2 h)$, we can deduce a $\eta_s \sim 0.26$. By assuming the same η_s for the case where heat recovery is employed, we can estimate our $GOR \sim 5.5$ given by the ratio between $F_{exp,HX} \sim 1.1\ kg/(m^2 h)$ and $F_{exp,NO-HX}$. Similarly, for the proposed stacked system of Fig. 2e,f the calculated flux rates, solar utilization efficiency and GOR are reported in the following figure. It should be noted that carbon black nanoparticles utilized here are extremely efficient light-heat converters[2], therefore we can argue that $\eta_s \approx \eta_t$. Future studies should also explore how to improve thermal efficiency.

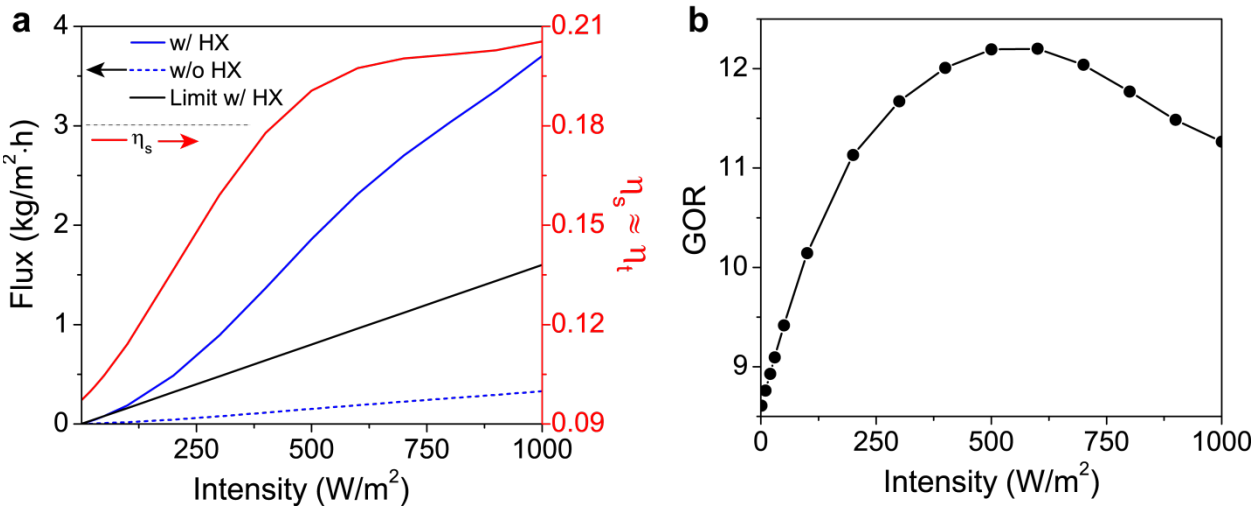

Supplementary Figure 11 – Efficiency analysis and GOR calculation for stacked system. a, Left y-axis: flux rates in the case of no heat recovery (blue, dashed), heat recovery (blue, solid) and theoretical limit for thermal desalination without heat recovery (black, solid) depending on incident irradiation for a n=10 stacked system, as analyzed in Fig. 2e,f. Right y-axis: extracted solar utilization efficiency obtained by taking the ratio between the calculated flux rates without heat recovery (blue, dashed) and the corresponding theoretical limit (black, solid). **b,** Calculated Gain Output Ratio (GOR) (red, solid) by taking the ratio between flux rates with (blue, solid) and without heat recovery (blue, dashed) assuming the solar efficiency.

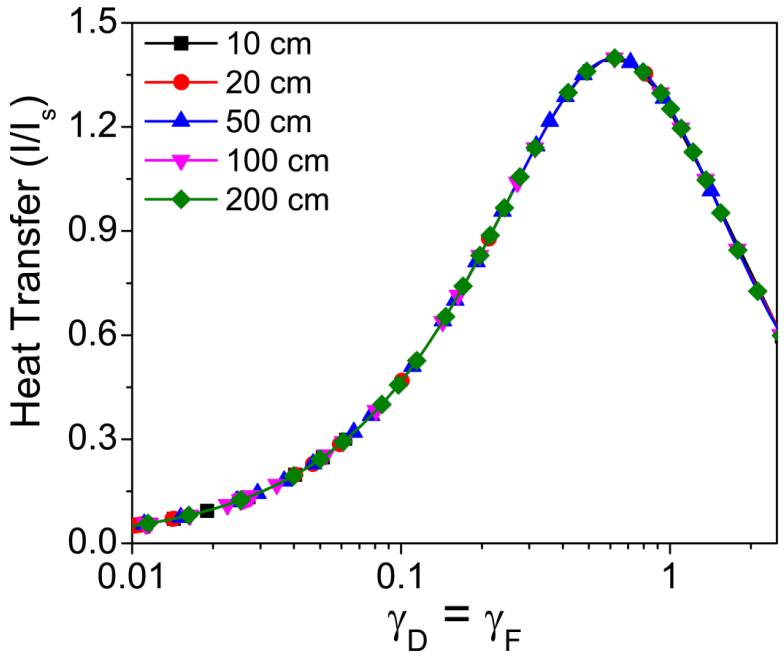

Supplementary Figure 12 - Heat transfer enhancements (normalized to I_s) of net heat transfers from F to D as a function of module lengths of 10 cm, 20 cm, 50 cm, 100 cm, 200 cm and fitting parameter gamma for the system.

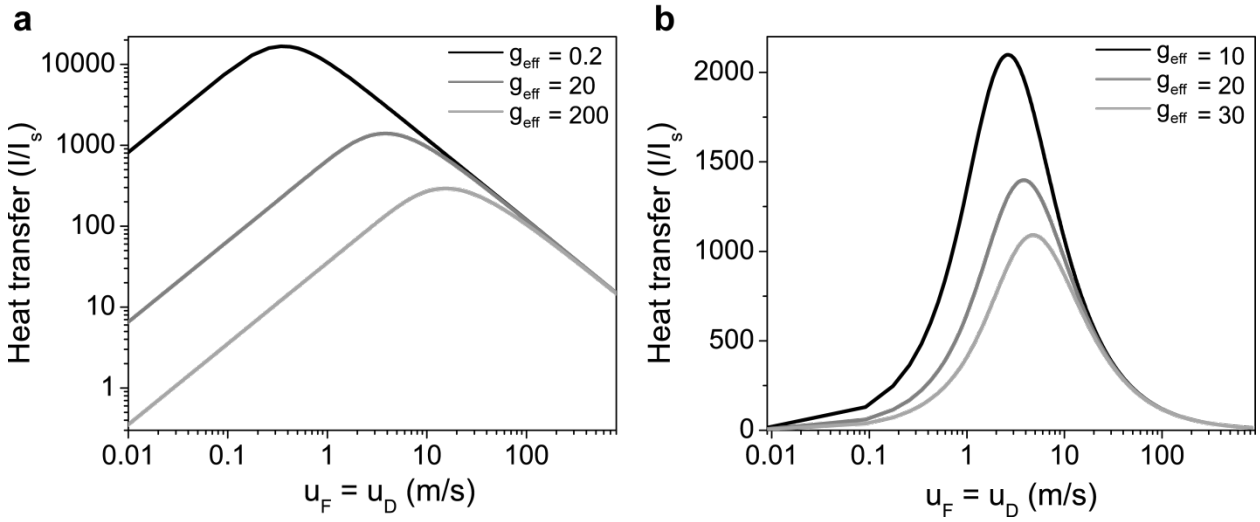

Supplementary Figure 13 - Heat transfer enhancements (normalized to I_s) of net heat transfers from F to D as a function of losses (g_{eff} values) in the system and equal feed and distillate flows for an analytically solved 1m system.

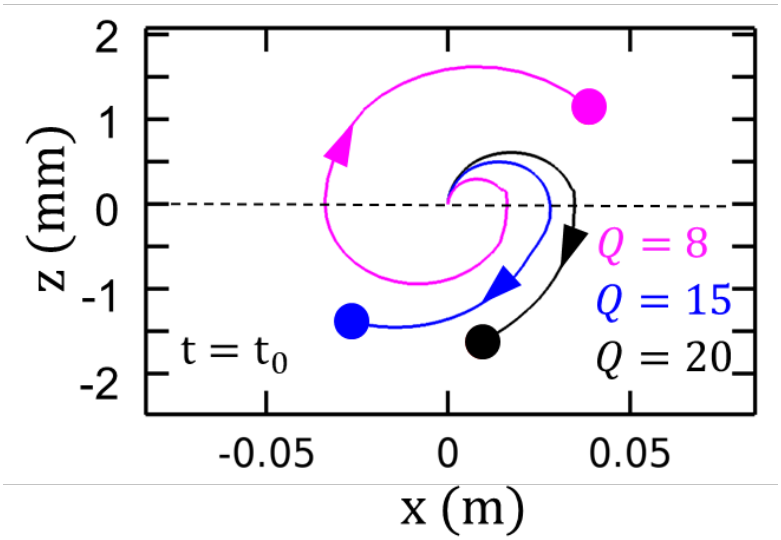

Supplementary Figure 14 –Probe trajectories in the TDO system at different resonant conditions. Snapshot of probe trajectories at a fixed time t_0 = 500 ns for $Q_F = Q_D$ = 8 mL/min (magenta), 15 mL/min (blue) and 20 mL/min (black).

Supplementary Note 7: Heat exchanger materials

For the experimental demonstration of thermal desalination oscillator (TDO) in this work we used commercially available thin copper or aluminum sheets as they are commonly used materials for heat exchange. We do observe oxide corrosion on the aluminum and copper sheets with long term operation. However, heat exchangers have been in use for several decades now and thus many new copper and aluminum alloys have been developed over the years that are corrosion resistant and compatible with waters of varying pH values. However, in the future the TDO system can be further optimized by implementing robust thermal conducting alloys. Also, a closer look at the thermal energy exchange in the system revels that the bottleneck in the heat transfer in our system is the low thermal conductivity of water compared to the heat exchanger material. Therefore, another more corrosion resistant material with comparatively higher thermal conductivity than water can also be used in future systems.

Supplementary figure 15 shows the effect of the reduction of the thermal conductivity, $k_{HX} = m_{COND} \times 400\ [W/(m \cdot K)]$, of the HX material, where m_{COND} is the multiplication factor that compares a given conductivity with the one we have used in this work. Given the relative low velocity of both feed and distillate fluids (<1 mm/s) in relation to the length of the HX (40.6 cm), the thermal conductivity has little effect on the heat recovery, unless it drops considerably ($m_{COND} < 0.001$). The small decrease in flux observed for high thermal conductivities is likely due to the well-insulated HX region, differently from the membrane region which is exposed to the environment through illumination window (see Supplementary Fig. 1). As consequence, a larger thermal conductivity implies that the heat is recycled closer to the membrane area, which is more exposed to external losses.

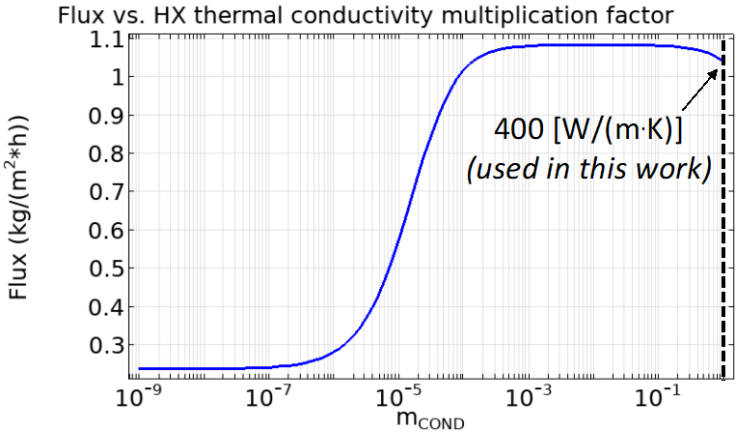

Supplementary Figure 15 – Calculated Flux versus multiplicative factor of the HX thermal conductivity $k_{HX} = m_{COND} \times 400\ [W/(m \cdot K)]$. The values refer to the experimental system shown in Fig. 1, at the resonant condition.

Supplementary Note 8: Avoiding salt accumulation and cleaning the system

For practical applications, the membrane can be cleaned by flowing purified water in the feed channel after several days of use to take away any salts. Also flowing heated water in the distillate channel and colder water in the feed channel when the salts are accumulated should also help clean the membrane as the water will now flow from bottom distillate to top feed and help in cleaning up any accumulated salts and refresh the system. This method of backwashing is common in cleaning reverse osmosis membranes[4].

Supplementary Note 9: Effect of water channel width on performance

Another parameter which affects solar desalination modules' efficiency is the thickness of the utilized channels, as it modifies the temperature vertical distribution and thus the overall energy balance of the system (see Fig. 2 in the main text). In supplementary fig. 16a we report the fresh water flux rate and maximum temperature in the system when the thickness of feed and distillate channels (w) is changed from ~0.5 mm to ~50 mm. Similarly to what shown in Fig. 2, this parameter also sizably affects the system performance, showing a peak at $w{\sim}1.6\,mm$. All experimental and simulation data reported in this work operated at $w{\sim}2\,mm$, quite close to the optimal value. In supplementary fig. 16b-d, we show temperature and heat flux vector fields for the case of $w{\sim}0.5\,mm, 1.6\,mm$ and $50\,mm$ respectively. Interestingly (similarly to what is shown in Fig. 2 of the main text) higher maximum temperatures do not necessarily correlate with a better performance as different losses can drain more input power when temperature increases.

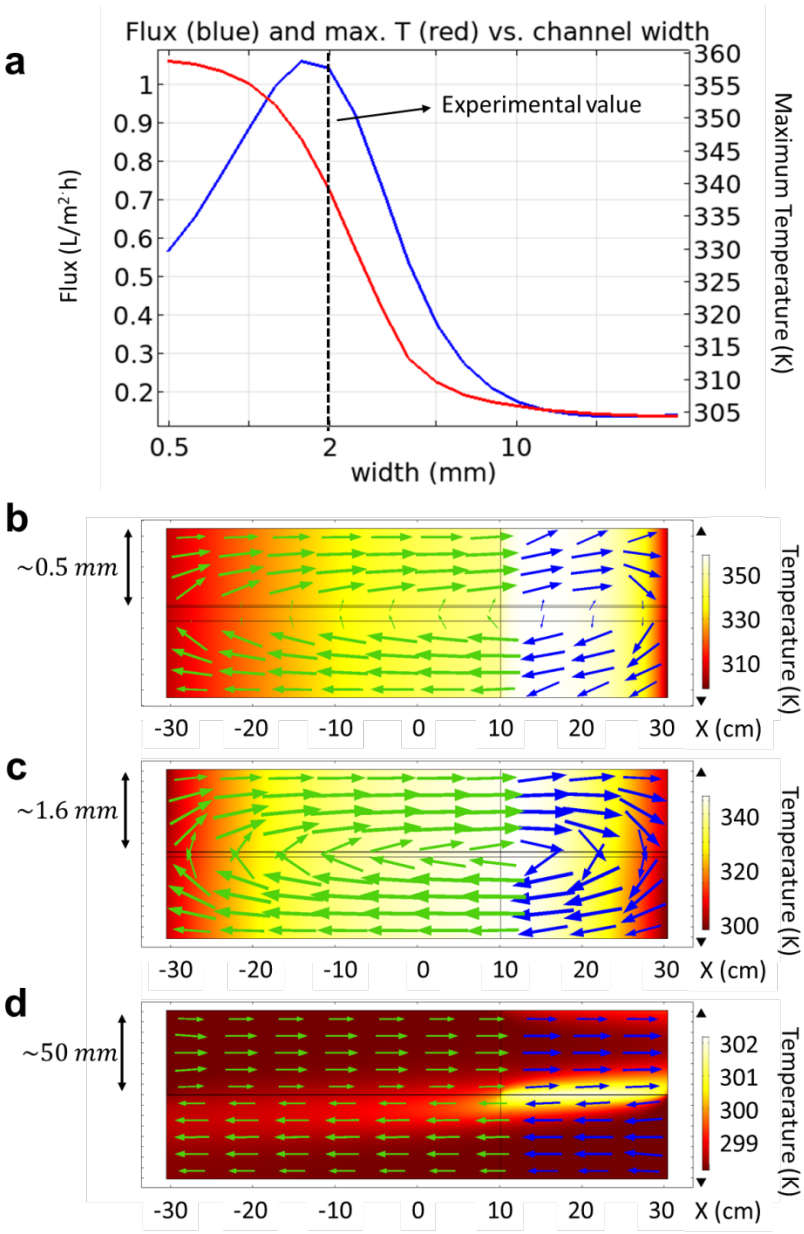

Supplementary figure 16 – Effect of channel thickness on NESMD+HX performance. **A**: flux rate (blue, left y-axis) and maximum temperature (red, right y-axis) dependence on feed and distillate channel thickness. The reference module is the one reported in Fig. 1 of the main text where we have fixed the input velocities of feed $v_f = 5.3 \cdot 10^{-4}\, m/s$ and distillate $v_d = 6.07 \cdot 10^{-4}\, m/s$. These values correspond to the utilized input velocities in the case of channel thickness (for both feed and distillate) $w = 2\, mm$ and input flow rates $Q_f = 6.5\, mL/min$ and $Q_d = 7.4\, mL/min$, which represent the flux rate maximum experimentally achieved in Fig. 1c. The width (third dimension, not shown in the plots) of the modules is $d = 0.1\, in$ in all the experiments and calculations reported in this work (in 2D simulations this parameter is utilized for proper input flow rates normalization). **B-D**: temperature maps (colors) and total heat flux vector field (arrows, same color code of main text) in the case of $w = 0.5\, mm, 1.6\, mm$ and $50\, mm$ respectively.

References

1 Dongare, P. D., Alabastri, A., Neumann, O., Nordlander, P. & Halas, N. J. Solar thermal desalination as a nonlinear optical process. *Proceedings of the National Academy of Sciences* **116**, 13182-13187, doi:10.1073/pnas.1905311116 (2019).

2 Dongare, P. D. *et al.* Nanophotonics-enabled solar membrane distillation for off-grid water purification. *Proceedings of the National Academy of Sciences* **114**, 6936-6941, doi:10.1073/pnas.1701835114 (2017).

3 Wang, Z. *et al.* Pathways and challenges for efficient solar-thermal desalination. *Science Advances* **5**, eaax0763, doi:10.1126/sciadv.aax0763 (2019).

4 Sagiv, A. & Semiat, R. Backwash of RO spiral wound membranes. *Desalination* **179**, 1-9, doi:https://doi.org/10.1016/j.desal.2004.11.050 (2005).